frontiers | Frontiers in Pharmacology

ORIGINAL RESEARCH
published: 15 July 2022
doi: 10.3389/fphar.2022.918819

Hyaluronic Acid–Stabilized Fe_3O_4 Nanoparticles for Promoting *In Vivo* Magnetic Resonance Imaging of Tumors

Weijie Zhang[1*†], *Zhongyue Zhang*[1†], *Shitong Lou*[1], *Zhiwei Chang*[1], *Baohong Wen*[2] and *Tao Zhang*[3]

[1]Department of Oncology, The First Affiliated Hospital of Zhengzhou University, Zhengzhou, China, [2]Department of MRI, The First Affiliated Hospital of Zhengzhou University, Zhengzhou, China, [3]College of Pharmacy, Xinxiang Medical University, Xinxiang, China

The use of iron oxide (Fe_3O_4) nanoparticles as novel contrast agents for magnetic resonance imaging (MRI) has attracted great interest due to their high r_2 relaxivity. However, both poor colloidal stability and lack of effective targeting ability have impeded their further expansion in the clinics. Here, we reported the creation of hyaluronic acid (HA)-stabilized Fe_3O_4 nanoparticles prepared by a hydrothermal co-precipitation method and followed by electrostatic adsorption of HA onto the nanoparticle surface. The water-soluble HA functions not only as a stabilizer but also as a targeting ligand with high affinity for the CD44 receptor overexpressed in many tumors. The resulting HA-stabilized Fe_3O_4 nanoparticles have an estimated size of sub-20 nm as observed by transmission electron microscopy (TEM) imaging and exhibited long-term colloidal stability in aqueous solution. We found that the nanoparticles are hemocompatible and cytocompatible under certain concentrations. As verified by quantifying the cellular uptake, the Fe_3O_4@HA nanoparticles were able to target a model cell line (HeLa cells) overexpressing the CD44 receptor through an active pathway. In addition, we showed that the nanoparticles can be used as effective contrast agents for MRI both *in vitro* in HeLa cells and *in vivo* in a xenografted HeLa tumor model in rodents. We believe that our findings shed important light on the use of active targeting ligands to improve the contrast of lesion for tumor-specific MRI in the nano-based diagnosis systems.

Keywords: iron oxide nanoparticles, magnetic resonance imaging, hyaluronic acid, HeLa cell/tumor, active targeting

OPEN ACCESS

Edited by:
Jianxun Ding,
Changchun Institute of Applied Chemistry (CAS), China

Reviewed by:
Wei Shao,
Westlake University, China
Wenbing Dai,
Peking University, China

***Correspondence:**
Weijie Zhang
fcczhangwj@zzu.edu.cn

[†]*These authors have contributed equally to this work*

Specialty section:
This article was submitted to Experimental Pharmacology and Drug Discovery, a section of the journal Frontiers in Pharmacology

Received: *12 April 2022*
Accepted: *27 May 2022*
Published: *15 July 2022*

Citation:
Zhang W, Zhang Z, Lou S, Chang Z, Wen B and Zhang T (2022) Hyaluronic Acid–Stabilized Fe_3O_4 Nanoparticles for Promoting In Vivo Magnetic Resonance Imaging of Tumors. Front. Pharmacol. 13:918819. doi: 10.3389/fphar.2022.918819

INTRODUCTION

Early and precise diagnosis is essential for treatment of cancer in the clinic, which continuously pushes the need for advanced imaging modalities and contrast agents. Magnetic resonance imaging (MRI) has been considered as one of the most effective and valuable *in vivo* bioimaging techniques because of its noninvasive and high-resolution features (Harisinghani et al., 2003; Sim et al., 2020). Traditional contrast agents for MRI are often small molecules with chelated metals (Caravan et al., 1999; Lohrke et al., 2016; Wahsner et al., 2019), such as Gd(III) or Mn(II). However, these molecular imaging agents suffer from rapid clearance and low efficiency due to their small-molecule nature (Lee et al., 2010). The emergence of nanotechnology has simulated the use of nanoparticles as novel

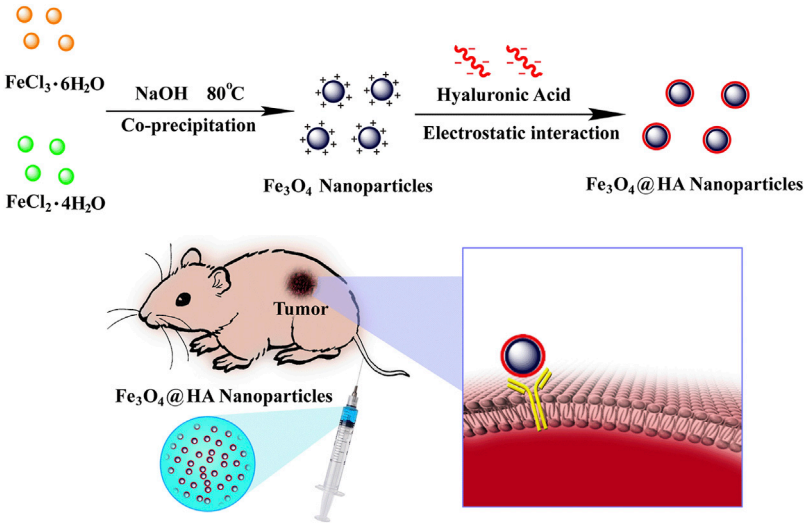

FIGURE 1 | Schematic illustration of synthesis and preparation of HA-stabilized Fe_3O_4 nanoparticles and Fe_3O_4@HA nanoparticles targeting the tumor *via* active binding with the receptor.

contrast agents and brought additional benefits due to the enhanced permeability and retention effect (EPR) (Hifumi et al., 2006; Bridot et al., 2007; Brigger et al., 2012; Oliveira et al., 2014; Swierczewska et al., 2016; Wei et al., 2017; Farzin et al., 2020; Leon-Janampa et al., 2020; Mitchell et al., 2021). Among them, iron oxide (Fe_3O_4) nanoparticles are the classic ones used in both T_1-weighted and T_2-weighted MRI (Ma et al., 2017; Shen et al., 2017). The ultrasmall ones with diameters smaller than 5 nm are used as positive contrast agents for T_1-weighted MRI, while the bigger ones larger than 10 nm are potentially used as negative contrast agents for T_2-weighted MRI due to their high r_2 relaxivity (Hu et al., 2011; Lee and Hyeon, 2012; Lee et al., 2015; Martinkova et al., 2018; Dadfar et al., 2019; Souri et al., 2022). Nevertheless, one major hurdle is that Fe_3O_4 nanoparticles easily aggregate and precipitate in the solution (Yu et al., 2006; Kim et al., 2011); the other one is that the use of bare Fe_3O_4 nanoparticles only benefits from passive targeting as a result of the EPR effect in leaky vasculature and poor lymphatic drainage (Maeda, 2010; Barreto et al., 2011; Luo et al., 2015). This approach does not apply for tumor-specific MRI. Therefore, to increase the efficiency and specificity, it is crucial to create stable nanoparticles with active tumor targeting properties.

Anchoring water-soluble polymers, for example, polyethylene glycol (PEG) (Yallapu et al., 2010; Hu et al., 2011; Li Z. et al., 2013; Luo et al., 2015), polyethyleneimine (PEI) (Mcbain et al., 2007; Liu et al., 2011; Li J. et al., 2013), chitosan (Zhi et al., 2006; Kievit et al., 2009; Shi et al., 2012; Khmara et al., 2019), and dextran (Tassa et al., 2011; Easo and Mohanan, 2013; Naha et al., 2019; Zhao et al., 2021), onto the surface of Fe_3O_4 nanoparticles is a proven strategy to stabilize the nanoparticles and avoid the formation of large aggregates on precipitation. Although this strategy could help to some extent, the functionalized Fe_3O_4 nanoparticles still lack the targeting ability. Hyaluronic acid (HA) is a water-soluble glycosaminoglycan with repeating units of D-glucuronic acid and N-acetyl-D-glucosamine (Lapcik et al., 1998; Choi et al., 2009; Della Sala et al., 2022). It is a natural polymer involved in many important physiological processes, such as wound healing, tissue regeneration, and joint lubrication. It has also been identified as a targeting auxiliary with high affinity for the CD44 receptor (Eliaz and Szoka, 2001; Toole, 2004; Ju et al., 2016; Lee et al., 2016), which is overexpressed in a variety of tumors. Therefore, HA could be used as a targeting ligand for both enhanced imaging and therapy (Lee et al., 2008a; Lee et al., 2008b; Li et al., 2014; Xiao et al., 2015; Zhang et al., 2020; Zhou et al., 2021).

With the aim of improving the contrast of lesions, we reported in this work the creation of HA-stabilized Fe_3O_4 nanoparticles and their applications in enhanced MRI of tumors. Fe_3O_4 nanoparticles were first synthesized *via* a co-precipitation method (Ding et al., 2016). The resulting nanoparticles possess positively charged surface chemistries, which were subsequently stabilized *via* HA through electrostatic interactions (**Figure 1**). Some literature reports have shown the modification of HA onto the surface of Fe_3O_4 nanoparticles by chemical conjugation (Li et al., 2014; Gong et al., 2019; Luo et al., 2019; Zhang et al., 2020). However, this method requires tedious chemical reactions, which could result in low yield, low functionalization density due to inefficient reaction, and batch-to-batch variations in modification density. Taking advantage of electrostatic interactions potentially contributes to the reproducibility of the system since the functionalization density mostly depends on the surface charge of the Fe_3O_4 nanoparticles. The HA-coated nanoparticles (Fe_3O_4@HA) were characterized with a variety of techniques, such as X-ray diffraction (XRD), Fourier transform infrared spectrometry (FTIR), thermogravimetric analysis (TGA), transmission electron microscopy (TEM), and dynamic light scattering (DLS), to verify the success in synthesis and stabilization. Through a series of *in vitro* studies, we showed that Fe_3O_4@HA nanoparticles are biocompatible and hemocompatible. We demonstrated the targeting ability of

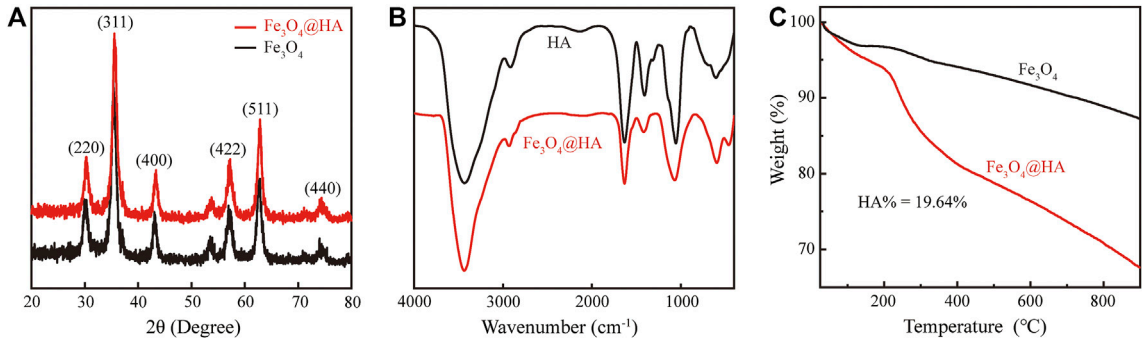

FIGURE 2 | Characterization of Fe_3O_4@HA nanoparticles. **(A)** XRD pattern of bare Fe_3O_4 and Fe_3O_4@HA nanoparticles. **(B)** FTIR curves of HA and Fe_3O_4@HA nanoparticles. **(C)** TGA analysis of bare Fe_3O_4 and Fe_3O_4@HA nanoparticles.

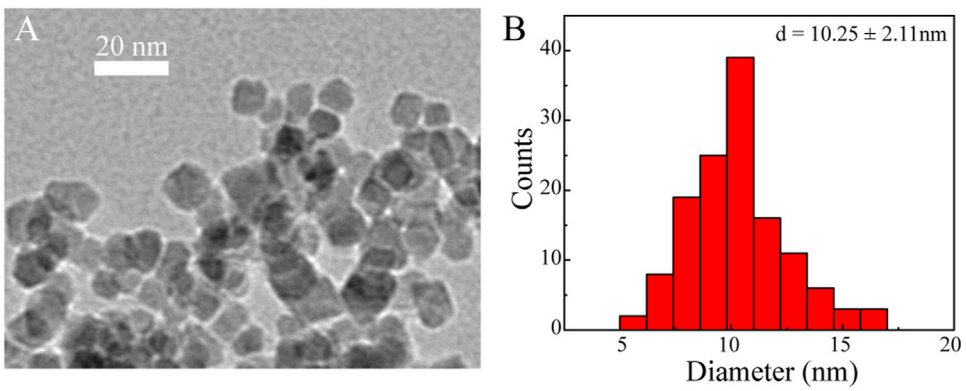

FIGURE 3 | Representative TEM image **(A)** and histogram of size distribution **(B)** of Fe_3O_4@HA nanoparticles. Spherical nanoparticles were observed with an estimated size of around 10.25 ± 2.11 nm (n = 132). As the particles were not stained, the HA corona was almost invisible. The actual size of Fe_3O_4@HA should be considered larger than the size measured here.

Fe_3O_4@HA nanoparticles at the cellular level *via* comparing cellular uptake of nanoparticles in HA active and blocked modes, respectively. More importantly, Fe_3O_4@HA showed much enhanced contrast for MRI in a cervical tumor model in rodents.

RESULTS AND DISCUSSION

Synthesis and Characterization of Fe_3O_4@HA Nanoparticles

Fe_3O_4 nanoparticles were first synthesized *via* a hydrothermal co-precipitation approach (Ding et al., 2016). HA was wrapped onto the surface of nanoparticles through electrostatic interactions (**Figure 1**). XRD was used to investigate the patterns of nanoparticles. Both bare Fe_3O_4 (black) and Fe_3O_4@HA (red) nanoparticles showed same peaks in (220), (311), (400), (422), (511), and (440) planes (**Figure 2A**), indicating that the incorporation of HA into the system happened in a physical absorption way rather than a chemical reaction. FTIR results (**Figure 2B**) showed the existence of characteristic signals of HA in Fe_3O_4@HA nanoparticles, suggesting successful functionalization of HA corona. Furthermore, TGA measurements were used to quantitatively identify the content of HA binding on the surface of Fe_3O_4@HA nanoparticles. Compared with bare Fe_3O_4 nanoparticles, the modified Fe_3O_4@HA nanoparticles exhibited an increase in weight loss from 12.75 to 32.39% (**Figure 2C**). The content of HA on the surface of nanoparticles is 19.64%. These results together indicate that we have successfully synthesized Fe_3O_4@HA nanoparticles with an HA loading of around 20% by weight.

We next characterized the morphology and size of the resulting Fe_3O_4@HA nanoparticles. TEM imaging clearly revealed spherical nanoparticles with a uniform size distribution (**Figure 3A**). The size of the nanoparticles was further measured by ImageJ and estimated to be around 10.25 ± 2.11 nm (**Figure 3B**). Since we did not stain the nanoparticles, the contrast of the HA corona should be relatively low and even negligible. Therefore, the size we measured here is possibly the size of bare Fe_3O_4 itself. The actual size of Fe_3O_4@HA should be considered larger than the size here with the extra HA corona. In addition, we examined the

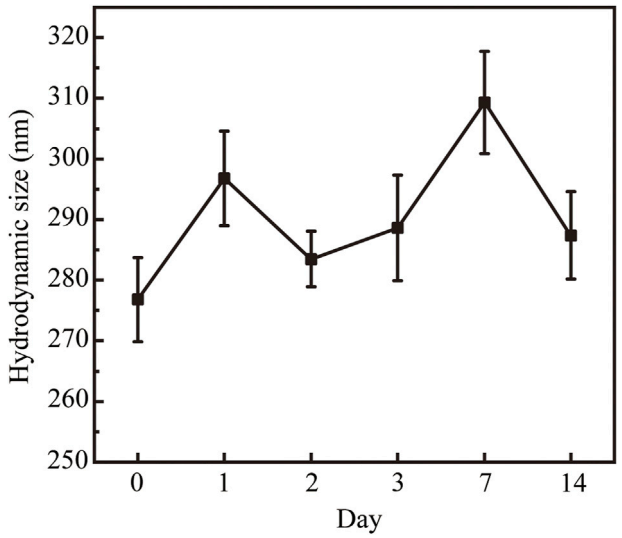

FIGURE 4 | Hydrodynamic size of the Fe_3O_4@HA nanoparticles and their physical stability over 14 days. As a result of slight aggregation, the hydrodynamic size is between 270–310 nm. Monitoring the hydrodynamic size over 14 days showed that the system was stable and did not form super large aggregations or precipitate out within 14 days. Data are calculated from three parallel measurements and presented as mean ± SD.

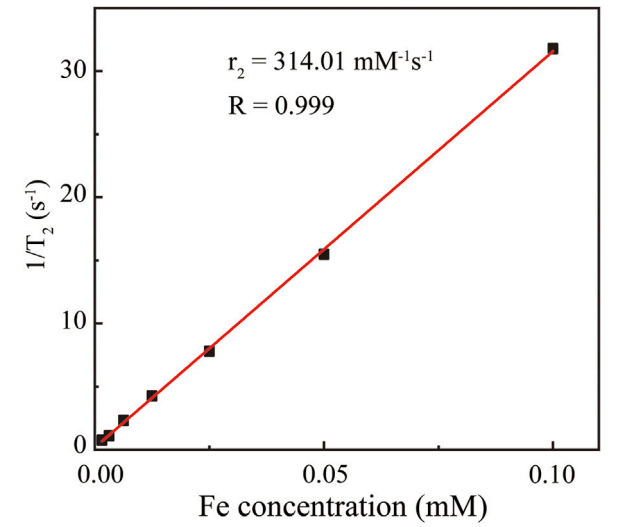

FIGURE 5 | Linear fitting of $1/T_2$ *vs*. Fe concentration. The Fe concentrations are 0.00156, 0.00313, 0.00625, 0.0125, 0.025, 0.05, and 0.1 mM. The resulting transverse relaxivity r_2 was estimated as 314.01 $mM^{-1}s^{-1}$.

hydrodynamic size and physical stability of Fe_3O_4@HA in PBS buffer *via* DLS. The results showed that the hydrodynamic size of Fe_3O_4@HA nanoparticles is in between 270–310 nm (**Figure 4**), which is much larger than the size measured by TEM. This is plausibly caused by slight aggregation or interaction among nanoparticles in the solution, as also observed by others in

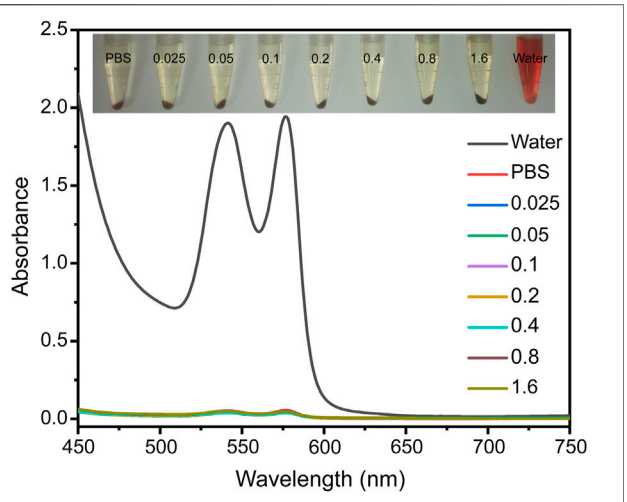

FIGURE 6 | Hemolysis assay of Fe_3O_4@HA nanoparticles was measured at Fe concentrations of 0.025, 0.05, 0.1, 0.2, 0.4, 0.8, and 1.6 mM with water and PBS as controls. The insert graph on the top is a photo of RBCs incubated with different solutions for 2 h and subsequently centrifuged. The UV-Vis absorptions of the supernatants were then collected.

similar systems (Li et al., 2014). The intensity averaged particle size measured by DLS often reflects a bit more on large-sized particles even though the majority are small ones (Fischer and Schmidt, 2016). With TEM imaging, we were able to identify the single nanoparticles. Monitoring the hydrodynamic size of Fe_3O_4@HA for 14 days (**Figure 4**) showed that the system did not form a super large aggregation or precipitate out within this period of time. Therefore, the bare Fe_3O_4 nanoparticles were successfully stabilized by coated HA. The zeta potential of Fe_3O_4@HA was measured as 32.3 ± 0.8 mV.

Measurements of T_2 Relaxivity of Fe_3O_4@HA Nanoparticles

Since magnetic Fe_3O_4 nanoparticles can shorten the transverse T_2 relaxation time of water protons so as to enhance the contrast, we next characterized the T_2 of protons in the Fe_3O_4@HA solutions of various Fe concentrations. The results (**Figure 5**) clearly showed that with the increase in the Fe concentration, Fe_3O_4@HA nanoparticles were able to cause a decrease in the magnetic resonance (MR) intensity in the T_2-weighted mode. The transverse relaxivity r_2 (the transverse relaxation rate per mM of iron) was further calculated by linear fitting of the relaxation rate $1/T_2$ *vs*. Fe concentration (**Figure 5**). The r_2 of the Fe_3O_4@HA nanoparticles was estimated at around 314 $mM^{-1}s^{-1}$. This number is higher than the numbers reported in the literature (Shi et al., 2008; Cai et al., 2012; Li J. et al., 2013; Li et al., 2014), which could be possibly caused by the thinner layer of HA corona due to electrostatic interactions compared with the chemical conjugated ones. Water molecules can penetrate easily through the thinner HA corona and interact with Fe_3O_4 in the core of the nanoparticles. These results suggested that Fe_3O_4@HA nanoparticles with such high r_2 can be used as a potential candidate for T_2-weighted MRI.

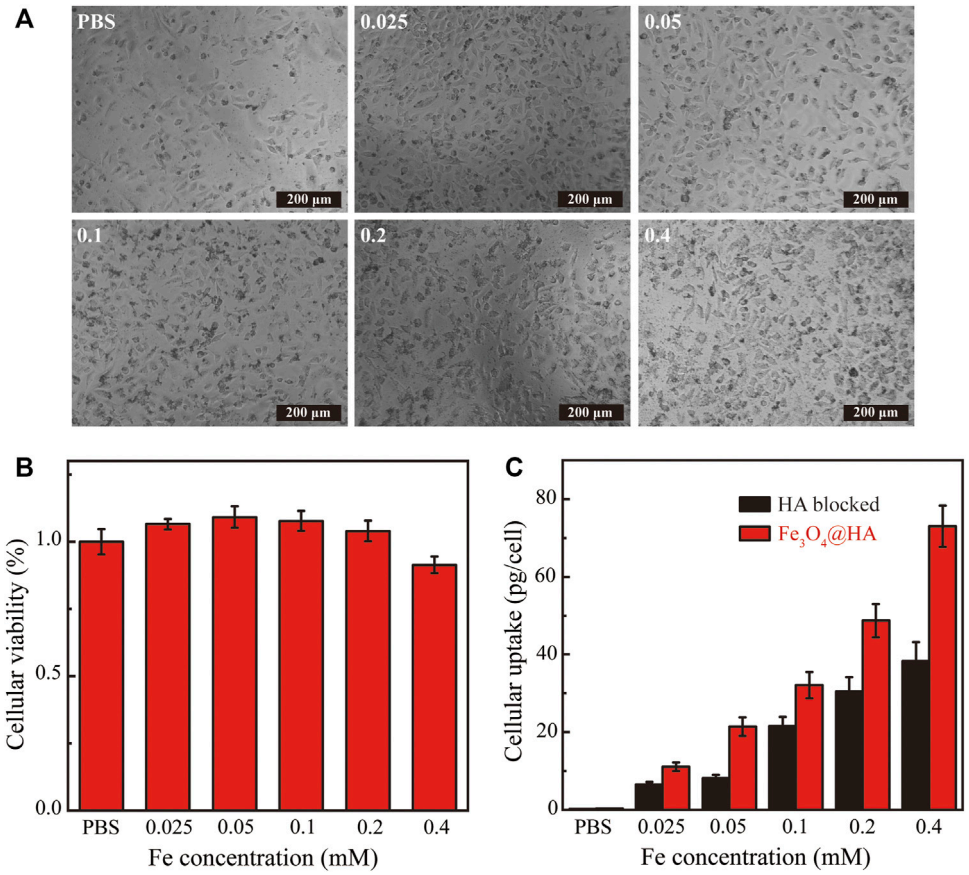

FIGURE 7 | (A) Phase contrast microscopic images of HeLa cells incubated with PBS and Fe_3O_4@HA nanoparticles at the Fe concentrations of 0.025, 0.05, 0.1, 0.2, and 0.4 mM, respectively. The morphologies of the nanoparticle groups were similar to those treated with PBS, and no obvious changes were observed. **(B)** *In vitro* cytotoxicity of Fe_3O_4@HA nanoparticles measured by MTT assay (n = 3 per group). Nanoparticles show no cytotoxicity until Fe concentration is at 0.2 mM. A slight decrease (less than 10%) in cell viability compared with the PBS group was observed at a Fe concentration of 0.4 mM. **(C)** Investigation of targeting ability and quantitative determination of cellular uptake of Fe_3O_4@HA nanoparticles using Hela cells (n = 3 per group). The HA blocked group is a negative control, in which HeLa cells were pretreated with HA to saturate the CD44 receptor and then incubated with Fe_3O_4@HA nanoparticles. The normal Fe_3O_4@HA group showed higher cellular uptake than the HA-blocked group at all concentrations, possibly through an active targeting mechanism. Data are presented as mean ± SD.

Hemolysis Measurements

Given that all the contrast agents are eventually used for *in vivo* detection and diagnosis, they should be extremely biocompatible with the body. We therefore investigated the hemocompatibility of the Fe_3O_4@HA nanoparticles, which is one of the crucial prerequisites before the *in vivo* studies. The hemolysis assay was performed at different Fe concentrations (0.025, 0.05, 0.1, 0.2, 0.4, 0.8, and 1.6 mM) with water and PBS as controls (**Figure 6**) for 2 h incubation at 37°C. The absorbents were collected after incubating Fe_3O_4@HA nanoparticles with RBC suspension (**Figure 6**). Along with PBS solution, we did not notice the strong hemolysis effect in the samples with Fe_3O_4@HA, while the water control showed an obvious hemolysis phenomenon. By comparing the absorbance at 541 nm, we found that the percentage of hemolysis is almost negligible (less than 3%) under the current Fe concentrations. Therefore, we concluded that our Fe_3O_4@HA nanoparticles were hemocompatible, warranting further investigation *in vivo*.

In Vitro Cytotoxicity Assay and Cellular Uptake

In order to function as imaging agents for living cells, the nanoparticles have to get into cells and also be compatible with cells. We therefore evaluated the cytotoxicity and cellular uptake of Fe_3O_4@HA nanoparticles. The nanoparticles at different Fe concentrations (0.025–0.4 mM) were incubated with HeLa cells for 24 h at 37°C. The morphologies of HeLa cells treated with Fe_3O_4@HA were observed by phase contrast microscopy. The images (**Figure 7A**) showed that the morphologies of the nanoparticle groups were similar to those treated with PBS, and no obvious changes were observed, indicating that Fe_3O_4@HA nanoparticles are compatible with cells under the current concentration range. This observation was further verified by *in vitro* cytotoxicity studies. The viabilities of HeLa cells were measured after incubation with Fe_3O_4@HA nanoparticles (0.025, 0.5, 0.1, 0.2, and 0.4 mM) for 24 h by MTT assay. Clearly, the Fe_3O_4@HA nanoparticles did not

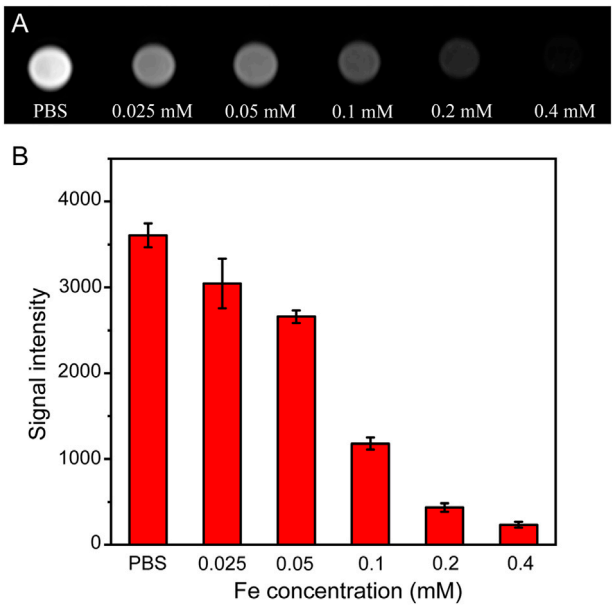

FIGURE 8 | (A) T_2-weighted *in vitro* MRI of HeLa cells treated with PBS and Fe_3O_4@HA nanoparticles at concentrations of 0.025, 0.05, 0.1, 0.2, and 0.4 mM for 6 h (n = 3). **(B)** Corresponding signal intensity of MRI results. Data are calculated from three parallel measurements and presented as mean ± SD.

exert any cytotoxicity until the Fe concentration was at 0.2 mM (**Figure 7B**). Further increase in the Fe concentration to 0.4 mM slightly decreased the cell viability by less than 10% compared with the cells treated with PBS. These results, together with the observation of cell morphology, demonstrated that Fe_3O_4@HA nanoparticles are biocompatible and almost non-cytotoxic at the Fe concentration up to 0.4 mM.

Since HA has high binding affinity with the CD44 receptor that is overexpressed in HeLa cells, we next assessed the targeting ability of HA toward the model HeLa cell line. Cells were treated with PBS and Fe_3O_4@HA nanoparticles at concentrations of 0.025, 0.5, 0.1, 0.2, and 0.4 mM. After 4 h of incubation, the cells were washed with PBS three times, digested, centrifuged, and resuspended in PBS for cell counting. Cells were further lysed, and the Fe uptake was quantified by inductively coupled plasma-atomic emission spectroscopy (ICP-AES). The negative control group was created by pretreating HeLa cells with HA (10 μM in DMEM) for 2 h to saturate the CD44 receptor and then incubating with Fe_3O_4@HA nanoparticles. As shown in **Figure 7C**, the HeLa cells showed a dose-dependent cellular uptake of Fe_3O_4@HA. The amount of nanoparticles entered the cells increased with increasing Fe concentration in both the Fe_3O_4@HA group and the negative control HA-blocked group. More importantly, the normal Fe_3O_4@HA group showed higher cellular uptake compared with the HA-blocked group at all concentrations. Quantitively, the amounts of Fe uptake in the Fe_3O_4@HA group were 1.7, 2.6, 1.5, 1.6, and 1.9 folds compared with those in the HA-blocked group at the incubation concentrations of 0.025, 0.5, 0.1, 0.2, and 0.4 mM,

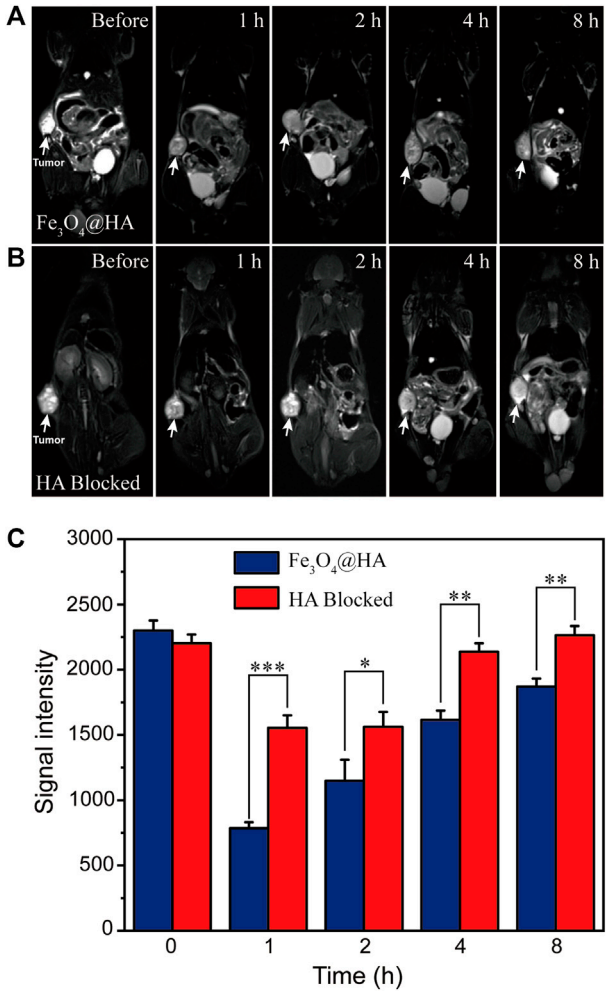

FIGURE 9 | (A,B) T_2-weighted *in vivo* MRI of nude mice (n = 3) bearing HeLa tumor before and after administration of Fe_3O_4@HA nanoparticles. The HA-blocked group **(B)** is a negative control, in which HA was intratumorally injected to saturate the CD44 receptor 1 h before administration of Fe_3O_4@HA nanoparticles. **(C)** Comparison of the corresponding signal intensity of MRI results of Fe_3O_4@HA and HA-blocked groups (n = 3 per group). The significant differences in the intensity indicate that Fe_3O_4@HA nanoparticles achieved more effective tumor targeting in the HA active state than in the HA blocked state. Data are presented as mean ± SD and analyzed by one-way ANOVA ($0.01 < {}^*p \le 0.05$; ${}^{**}p \le 0.01$; ${}^{***}p \le 0.001$).

respectively (**Figure 7C**). These observations suggested that the HA corona on the surface of Fe_3O_4@HA nanoparticles can mediate the specific interactions with the CD44 receptor expressed by HeLa cells and realize an active targeting mechanism. The results also perfectly elaborate on the design principle of the work.

In Vitro MRI of HeLa Cells

To verify the feasibility of using Fe_3O_4@HA nanoparticles as contrast agents, we next performed an *in vitro* MRI study. HeLa cells were co-incubated with Fe_3O_4@HA nanoparticles at various Fe concentrations (0.025, 0.5, 0.1, 0.2, and 0.4 mM) for 6 h at 37°C with PBS as a control. Furthermore, T_2-weighted MRI of the

HeLa cells was performed and analyzed. As shown in **Figure 8A**, the MR images of the cells treated with Fe_3O_4@HA presented lower signal intensity than the PBS control group. The signal also exhibited a dose-dependent behavior, which decreased with the increase in the Fe concentration (**Figure 8B**). These results indicated the effective role of Fe_3O_4@HA nanoparticles in providing adequate imaging contrast, and the dose-dependent decrease in signal intensity is probably a result of the concentration-dependent cellular uptake.

In Vivo MRI in a Xenografted Tumor Model in Mice

After demonstrating the possibility of *in vitro* MRI in cells, we further investigated the use of Fe_3O_4@HA nanoparticles for *in vivo* MRI in a HeLa xenografted tumor model. When the tumor reached a size of around 150 mm^3, Fe_3O_4@HA nanoparticles were administered intravenously at Fe concentration of 10 mM in 100 μL PBS. MRI was then performed at 1, 2, 4 and 8 h post-injection. In the group of blocked HA, it (100 μM in 50 μL PBS) was intratumorally injected to saturate the CD44 receptor 1 h before administration of nanoparticles. The T_2-weighted MR images of Fe_3O_4@HA and HA-blocked groups are shown in **Figures 9A,B**, respectively. We found that the MR signals in both groups decreased after injection. Based on more quantitative assessment (**Figure 9C**), we found that the highest contrast enhancement happened at 1 h post injection and then gradually recovered. In the Fe_3O_4@HA group, the signals decreased by 66, 50, 30, and 20% at 1, 2, 4, and 8 h post-injection, respectively, compared with that before injection. However, in the HA-blocked group, the signals only decreased by 29% at 1 h post injection and had already recovered back to similar intensity as that before injection at 4 h. Direct comparison between Fe_3O_4@HA and HA-blocked groups showed significant differences, indicating that Fe_3O_4@HA nanoparticles achieved more effective tumor targeting in the HA active state than in the HA-blocked state. The slight decrease in the MR intensity in the HA-blocked group could be a result of passive targeting because of the EPR effect, and the recovery of the intensity could be mainly attributed to the metabolism process that cleared nanoparticles out of the body, but the significantly lower MR signals in the Fe_3O_4@HA group than in the HA blocked group at the same time point clearly indicated the role of the HA-mediated specific tumor targeting pathway in addition to the EPR effect. These results are consistent with our *in vitro* cellular uptake studies, which again confirmed that Fe_3O_4@HA nanoparticles could target the tumor through an active targeting mechanism, realizing more effective MRI both *in vitro* and *in vivo*.

CONCLUSION

In this article, we created the HA-stabilized Fe_3O_4 nanoparticles simply through electrostatic interactions. The adhesion of HA onto the surface of bare Fe_3O_4 nanoparticles contributes to the dispersibility and stability of colloidal aggregates. The formed Fe_3O_4@HA nanoparticles are compatible with cancer cells and RBC suspension in the studied concentration range. The relatively high r_2 relaxivity is a result of the thin-layered HA corona that allows better penetration of water molecules into the particle core. Our findings showed that Fe_3O_4@HA nanoparticles are able to enter into HeLa cells overexpressing the CD44 receptor through a specific cell targeting pathway in the HA active state compared with the HA-blocked state. Furthermore, the created Fe_3O_4@HA nanoparticles can be used as effective nanoprobes for targeted MRI of both HeLa cells *in vitro* and xenografted HeLa tumors *in vivo*. We hope that our findings will eventually contribute to building up the general design principle of the targeted delivery of nanoparticles for both cancer diagnosis and therapy.

MATERIALS AND METHODS

Materials

Hyaluronic acid (6 KDa) was purchased from Zhenjiang Dong Yuan Biotechnology Corporation (Zhenjiang, China). Iron (III) chloride hexahydrate ($FeCl_3.6H_2O$), iron (II) chloride tetrahydrate ($FeCl_2.4H_2O$), and sodium hydroxide were purchased from Aladdin Ltd. (Shanghai, China). 3-(4,5Dimethylthiazol-2-yl)-2,5-diphenyltetrazolium bromide (MTT) was supplied by Thermo Fisher Scientific, Ltd. (Waltham, MA). Fetal bovine serum (FBS), Dulbecco's modified Eagle's medium (DMEM), penicillin-streptomycin, and trypsin were obtained from Gibco Life Technologies Co. (Grand Island, NY). Regenerated cellulose dialysis membranes with a molecular weight cut-off (MWCO) of 50 KDa were acquired from Fisher (Pittsburgh, PA).

Synthesis of Fe3O4@HA Nanoparticles

The nanoparticles were synthesized *via* a facile controlled co-precipitation method. Briefly, 30 mg of HA was first dissolved in 25 ml Milli-Q water (resistivity higher than 18.2 MΩ cm, a Milli-Q Plus 185 water purification system (Millipore, Bedford, MA)) and stirred in a three-neck round-bottom flask to obtain a homogeneous solution. The solution was degassed with bubbling N_2 to remove O_2 and heated to 80°C. Then, 0.36 g of $FeCl_3.6H_2O$ and 0.132 g of $FeCl_2.4H_2O$ were dissolved in 7.5 ml O_2-free Milli-Q water and added to the HA solution. After stirring for 15 min under N_2 protection, 10 ml of O_2-free Milli-Q water containing 1 g of NaOH was quickly added to the mixture under mechanical stirring of 1200 rpm. The reaction was continued for another 2 h at 80°C. After cooling down to room temperature, the black solution was 1) centrifuged at a low speed of 600 rpm to get rid of the big aggregations and 2) magnetically separated and re-dispersed in the Milli-Q water. The obtained solution was further dialyzed (molecular weight cut-off at 50 KDa) against Milli-Q water for 2 days to remove free ions and HA. A small quantity of the Fe_3O_4@HA solution was subjected to freeze-drying, and the leftover was stored at 4°C.

Characterization of Fe_3O_4@HA Nanoparticles

The crystalline structure of the Fe_3O_4 and Fe_3O_4@HA nanoparticles was characterized by X-ray diffraction (XRD) in

a 2θ range of 20–80°, using a D/max 2550 PC X-ray diffractometer (Japan, Rigaku Cop.) with Cu Kα radiation (λ = 0.154,056 nm) at 40 kV and 200 mA. Fourier transform infrared (FTIR) spectra of Fe_3O_4 and Fe_3O_4@HA nanoparticles were obtained by using a Nexus 670 spectrometer (Thermo Nicolet Corporation, Madison, WI). Thermogravimetric analysis (TGA) was performed in a temperature range of 30–900°C with a heating rate of 20°C/min under nitrogen using a TG209 F1 (NETZSCH Instruments Co., Ltd., Germany) thermogravimetric analyzer.

Size and Stability Measurements

The TEM samples were prepared by adding 10 μL of Fe_3O_4@HA nanoparticle (Fe concentration 0.1 mM) solution onto a carbon-film-coated copper grid (400 square mesh, Electron Microscopy Sciences, Hatfield, PA, United States), and the excess solution was wicked with a filter paper. The grid was air-dried before imaging and was then imaged using a FEI Tecnai 12 TWIN transmission electron microscope (100 kV). A SIS Megaview III wide-angle CCD camera was used to acquire the TEM images. The samples for dynamic light scattering measurements were prepared at a Fe concentration of 0.2 mM, and then, the hydrodynamic size of Fe_3O_4@HA nanoparticles was measured by a Malvern Zetasizer Nano ZS model ZEN3600 (Worcestershire, U.K.) equipped with a standard 633-nm laser. Three repeated measurements for each sample were determined to give the average values and standard deviations.

Determination of T_2 Relaxivity

The Fe concentration of Fe_3O_4@HA nanoparticles was previously determined using the Leeman Prodigy Inductively Coupled Plasma-Atomic Emission Spectroscopy (ICP-AES) system (Hudson, NH03051). Sample solutions at Fe concentrations of 0.00156, 0.00313, 0.00625, 0.0125, 0.025, 0.05, and 0.1 mM were prepared by dilution of stock solution before measurements. T_2 relaxometry was performed by using a 0.5-T NMI20-Analyst NMR Analyzing and Imaging system (Shanghai Niumag Corporation, China). Instrumental parameters are as follows: a point resolution of 156 mm × 156 mm, section thickness of 0.6 mm, TR of 4000 ms, TE of 60 ms, and number of excitation of 1. The T_2 relaxivity was determined by linear fitting of $1/T_2$ *vs.* Fe concentration.

Hemolysis Assay

Mouse blood (1.5 ml) collected from the inner canthus vein plexus was mixed with 3.5 ml of PBS. Pure red blood cells (RBCs) were obtained *via* repeated centrifugation/redispersion processes (2000 rpm, 10 min, three times). The RBCs were then diluted with 5 ml of PBS for further use. A measure of 100 μL of the obtained RBC suspension was mixed with 900 μL PBS (negative control), water (positive control), and Fe_3O_4@HA nanoparticle solution in PBS at various Fe concentrations (0.025, 0.05, 0.1, 0.2, 0.4, 0.8, and 1.6 mM). After 2 h incubation at 37°C, sample solutions were centrifuged at 10,000 rpm for 15 min. The absorbance of the supernatant for each sample at 540 nm was then measured *via* a Lambda 25 UV-Vis spectrophotometer (PerkinElmer, Boston, MA). The hemolysis rate was calculated as follows: $\text{hemolysisrate}(\%) = (A_{(\text{sample, 540 nm})} - A_{(\text{negative, 540 nm})})/(A_{(\text{positive, 540 nm})} - A_{(\text{negative, 540 nm})}) \times 100\%$.

Cell Culture, Morphology, and *In Vitro* Cytotoxicity

HeLa cells were purchased from the Institute of Biochemistry and Cell Biology (the Chinese Academy of Sciences, Shanghai, China) and cultured in DMEM containing 5% FBS and 1% antibiotics at 37°C and 5% CO_2.

HeLa cells (10,000 cells/well) were seeded in 96-well plates overnight. The Fe_3O_4@HA nanoparticles at various Fe concentrations (0.025, 0.05, 0.1, 0.2, and 0.4 mM) were next incubated with the HeLa cells for another 24 h in 200 μL of DMEM. HeLa cells treated with PBS were used as a control. The morphology of HeLa cells was further observed by phase contrast microscopy (Leica DM IL LED inverted phase contrast microscope) at a magnification of 200 times.

In vitro cytotoxicity was further quantitively confirmed by the MTT assay. Similar to the protocols described earlier, HeLa cells (10,000 cells/well) were seeded in 96-well plates overnight. The Fe_3O_4@HA nanoparticles at various Fe concentrations (0.025, 0.05, 0.1, 0.2, and 0.4 mM) were then incubated with the HeLa cells for another 24 h in 200 μL DMEM. Furthermore, the cells were rinsed three times with PBS and then incubated in 100 μL of FBS-free DMEM medium containing 10% MTT for 4 h. After removal of the medium, the MTT assay was performed according to the manufacturer's instructions. For each concentration, three parallel wells were measured to give the average values and standard deviations.

Cellular Uptake of Fe3O4@HA in HA Active and Blocked States

HeLa cells (2×10^6 cells/well) were seeded in 6-well plates for overnight adherence. The seeded plates were divided into two groups, and the cell medium was replaced on the second day. One group was replaced with fresh DMEM medium, and the other group was replaced with fresh DMEM containing HA (10 μM) that pre-saturates the overexpressed CD44 receptor in HeLa cells. After incubation for another 2 h, the medium was removed, and the cells were washed with PBS three times. Then, the cells were further incubated with fresh DMEM containing Fe_3O_4@HA nanoparticles at various Fe concentrations (0.025, 0.05, 0.1, 0.2, and 0.4 mM) for 4 h at 37°C. Next, the cells were washed three times with PBS, digested by trypsinization, centrifuged (1000 rpm, 5 min), and resuspended in PBS for cell counting. The remaining cells were centrifuged (1000 rpm, 5 min) and lysed using 0.5 ml aqua regia solution (nitric acid/hydrochloric acid, v/v = 1:3) for one day. Finally, we diluted the samples with PBS, and the cellular uptake of the Fe_3O_4@HA nanoparticles was evaluated by inductively coupled plasma-atomic emission spectroscopy (ICP-AES).

In Vitro MRI of Cancer Cells

The animal study protocol was approved by the Ethics Committee of Scientific Research and Clinical Trials of the First Affiliated Hospital of Zhengzhou University. HeLa cells (5×10^6 cells/flask) were seeded into 25 cm^2 culture flasks with 5 ml DMEM overnight at 37°C. On the second day, Fe_3O_4@HA

nanoparticles at different Fe concentrations (0.025, 0.05, 0.1, 0.2, and 0.4 mM) in 5 ml fresh medium were replaced. After 6 h incubation, the HeLa cells were rinsed three times with PBS, digested by trypsinization, centrifuged (1000 rpm, 5 min), and resuspended in 1 ml (containing 0.5% agarose) PBS in a 2-ml eppendorf tube. The T_2-weighted MRI of HeLa cells was performed on a 3.0 T Signa HDxt superconductor clinical MR system (GE Medical Systems, Fairfield, CT). 2D spin-echo MR images were obtained with the parameters of 2 mm slice thickness, TR/TE 2000/96.2 ms, FOV 6 × 6 cm, and 256 × 256 matrix.

In Vivo MRI of the Tumor Model

For the experiment, 6-week-old female BALB/c nude mice were purchased from SPF (Beijing) Biotechnology Co., Ltd. HeLa cells (2×10^6 in 100 ml PBS) were subcutaneously injected into the left back of the mice. After 3–4 weeks, when the tumor reached a size ~150 mm^3, the mice were randomly divided into two groups (n = 3 per group). One group was intratumorally injected with HA (100 μM) in 50 μL PBS 1 h before the injection of Fe_3O_4@HA contrast agents. Then, both groups of mice were anesthetized by an intraperitoneal injection of pentobarbital sodium (40 mg/kg). The Fe_3O_4@HA nanoparticles (Fe concentration = 10 mM, in 100 μL PBS) were then intravenously injected into mice. The *in vivo* tumor MRI studies were conducted at different time points (1, 2, 4, and 8 h post injection) using a 3.0 T Signa HDxt superconducting clinical MR system attached with a custom-built animal receiver coil. 2D spin-echo MR images were obtained with the parameters of 2 mm slice thickness, TR/TE 2000/96.2 ms, FOV 6 × 6 cm, and 256 × 256 matrix. The T_2-weighted MR images before administration were also obtained as controls.

DATA AVAILABILITY STATEMENT

The raw data supporting the conclusion of this article will be made available by the authors without undue reservation.

ETHICS STATEMENT

The animal study was reviewed and approved by the Ethics Committee of Scientific Research and Clinical Trials of the First Affiliated Hospital of Zhengzhou University.

AUTHOR CONTRIBUTIONS

WZ convinced the idea, designed, and supervised the experiments; ZZ, SL, ZC, BW, and TZ conducted the experiments; WZ, ZZ, and BW analyzed the data; WZ and ZZ wrote the manuscript. All authors have read and agreed to the published version of the manuscript.

FUNDING

This research was funded by the Henan Province Medical Science and Technology Research Program (Provincial and Ministry Co-construction) Project, grant number SBGJ202003026.

REFERENCES

Barreto, J. A., O'malley, W., Kubeil, M., Graham, B., Stephan, H., and Spiccia, L. (2011). Nanomaterials: Applications in Cancer Imaging and Therapy. *Adv. Mater* 23, H18–H40. doi:10.1002/adma.201100140

Bridot, J. L., Faure, A. C., Laurent, S., Rivière, C., Billotey, C., Hiba, B., et al. (2007). Hybrid Gadolinium Oxide Nanoparticles: Multimodal Contrast Agents for *In Vivo* Imaging. *J. Am. Chem. Soc.* 129, 5076–5084. doi:10.1021/ja068356j

Brigger, I., Dubernet, C., and Couvreur, P. (2012). Nanoparticles in Cancer Therapy and Diagnosis. *Adv. Drug Deliv. Rev.* 64, 24–36. doi:10.1016/j.addr.2012.09.006

Cai, H., Li, K., Shen, M., Wen, S., Luo, Y., Peng, C., et al. (2012). Facile Assembly of Fe_3O_4@Au Nanocomposite Particles for Dual Mode Magnetic Resonance and Computed Tomography Imaging Applications. *J. Mat. Chem.* 22, 15110–15120. doi:10.1039/c2jm16851k

Caravan, P., Ellison, J. J., Mcmurry, T. J., and Lauffer, R. B. (1999). Gadolinium(III) Chelates as MRI Contrast Agents: Structure, Dynamics, and Applications. *Chem. Rev.* 99, 2293–2352. doi:10.1021/cr980440x

Choi, K. Y., Min, K. H., Na, J. H., Choi, K., Kim, K., Park, J. H., et al. (2009). Self-assembled Hyaluronic Acid Nanoparticles as a Potential Drug Carrier for Cancer Therapy: Synthesis, Characterization, and *In Vivo* Biodistribution. *J. Mat. Chem.* 19, 4102–4107. doi:10.1039/b900456d

Dadfar, S. M., Roemhild, K., Drude, N. I., Von Stillfried, S., Knüchel, R., Kiessling, F., et al. (2019). Iron Oxide Nanoparticles: Diagnostic, Therapeutic and Theranostic Applications. *Adv. Drug Deliv. Rev.* 138, 302–325. doi:10.1016/j.addr.2019.01.005

Della Sala, F., Fabozzi, A., Di Gennaro, M., Nuzzo, S., Makvandi, P., Solimando, N., et al. (2022). Advances in Hyaluronic-Acid-Based (Nano)Devices for Cancer Therapy. *Macromol. Biosci.* 22, e2100304. doi:10.1002/mabi.202100304

Ding, L., Hu, Y., Luo, Y., Zhu, J., Wu, Y., Yu, Z., et al. (2016). LAPONITE (R)-stabilized Iron Oxide Nanoparticles for *In Vivo* MR Imaging of Tumors. *Biomater. Sci.* 4, 474–482. doi:10.1039/c5bm00508f

Easo, S. L., and Mohanan, P. V. (2013). Dextran Stabilized Iron Oxide Nanoparticles: Synthesis, Characterization and *In Vitro* Studies. *Carbohydr. Polym.* 92, 726–732. doi:10.1016/j.carbpol.2012.09.098

Eliaz, R. E., and Szoka, F. C. (2001). Liposome-encapsulated Doxorubicin Targeted to CD44: A Strategy to Kill CD44-Overexpressing Tumor Cells. *Cancer Res.* 61, 2592–2601.

Farzin, A., Etesami, S. A., Quint, J., Memic, A., and Tamayol, A. (2020). Magnetic Nanoparticles in Cancer Therapy and Diagnosis. *Adv. Healthc. Mater* 9, e1901058. doi:10.1002/adhm.201901058

Fischer, K., and Schmidt, M. (2016). Pitfalls and Novel Applications of Particle Sizing by Dynamic Light Scattering. *Biomaterials* 98, 79–91. doi:10.1016/j.biomaterials.2016.05.003

Gong, T., Dong, Z., Fu, Y., Gong, T., Deng, L., and Zhang, Z. (2019). Hyaluronic Acid Modified Doxorubicin Loaded Fe_3O_4 Nanoparticles Effectively Inhibit Breast Cancer Metastasis. *J. Mater Chem. B* 7, 5861–5872. doi:10.1039/c9tb01250h

Harisinghani, M. G., Barentsz, J., Hahn, P. F., Deserno, W. M., Tabatabaei, S., Van De Kaa, C. H., et al. (2003). Noninvasive Detection of Clinically Occult Lymph-Node Metastases in Prostate Cancer. *N. Engl. J. Med.* 348, 2491–2499. doi:10.1056/NEJMoa022749

Hifumi, H., Yamaoka, S., Tanimoto, A., Citterio, D., and Suzuki, K. (2006). Gadolinium-based Hybrid Nanoparticles as a Positive MR Contrast Agent. *J. Am. Chem. Soc.* 128, 15090–15091. doi:10.1021/ja066442d

Hu, F., Jia, Q., Li, Y., and Gao, M. (2011). Facile Synthesis of Ultrasmall PEGylated Iron Oxide Nanoparticles for Dual-Contrast T1- and T2-Weighted Magnetic Resonance Imaging. *Nanotechnology* 22, 245604. doi:10.1088/0957-4484/22/24/245604

Ju, Y., Dai, Q., Cui, J., Dai, Y., Suma, T., Richardson, J. J., et al. (2016). Improving Targeting of Metal-Phenolic Capsules by the Presence of Protein Coronas. *ACS Appl. Mater Interfaces* 8, 22914–22922. doi:10.1021/acsami.6b07613

Khmara, I., Strbak, O., Zavisova, V., Koneracka, M., Kubovcikova, M., Antal, I., et al. (2019). Chitosan-stabilized Iron Oxide Nanoparticles for Magnetic Resonance Imaging. *J. Magnetism Magnetic Mater.* 474, 319–325. doi:10.1016/j.jmmm.2018.11.026

Kievit, F. M., Veiseh, O., Bhattarai, N., Fang, C., Gunn, J. W., Lee, D., et al. (2009). PEI-PEG-Chitosan Copolymer Coated Iron Oxide Nanoparticles for Safe Gene Delivery: Synthesis, Complexation, and Transfection. *Adv. Funct. Mater* 19, 2244–2251. doi:10.1002/adfm.200801844

Kim, B. H., Lee, N., Kim, H., An, K., Park, Y. I., Choi, Y., et al. (2011). Large-scale Synthesis of Uniform and Extremely Small-Sized Iron Oxide Nanoparticles for High-Resolution T1 Magnetic Resonance Imaging Contrast Agents. *J. Am. Chem. Soc.* 133, 12624–12631. doi:10.1021/ja203340u

Lapcík L Jr and, L., Lapcík, L., De Smedt, S., Demeester, J., and Chabrecek, P. (1998). Hyaluronan: Preparation, Structure, Properties, and Applications. *Chem. Rev.* 98, 2663–2684. doi:10.1021/cr941199z

Lee, H., Lee, K., Kim, I. K., and Park, T. G. (2008a). Synthesis, Characterization, and *In Vivo* Diagnostic Applications of Hyaluronic Acid Immobilized Gold Nanoprobes. *Biomaterials* 29, 4709–4718. doi:10.1016/j.biomaterials.2008.08.038

Lee, H., Lee, K., and Park, T. G. (2008b). Hyaluronic Acid-Paclitaxel Conjugate Micelles: Synthesis, Characterization, and Antitumor Activity. *Bioconjug Chem.* 19, 1319–1325. doi:10.1021/bc8000485

Lee, H., Yang, S. H., Heo, D., Son, H., Haam, S., Suh, J. S., et al. (2016). Molecular Imaging of CD44-Overexpressing Gastric Cancer in Mice Using T2 MR Imaging. *J. Nanosci. Nanotechnol.* 16, 196–202. doi:10.1166/jnn.2016.11782

Lee, N., and Hyeon, T. (2012). Designed Synthesis of Uniformly Sized Iron Oxide Nanoparticles for Efficient Magnetic Resonance Imaging Contrast Agents. *Chem. Soc. Rev.* 41, 2575–2589. doi:10.1039/c1cs15248c

Lee, N., Yoo, D., Ling, D., Cho, M. H., Hyeon, T., and Cheon, J. (2015). Iron Oxide Based Nanoparticles for Multimodal Imaging and Magnetoresponsive Therapy. *Chem. Rev.* 115, 10637–10689. doi:10.1021/acs.chemrev.5b00112

Lee, S., Xie, J., and Chen, X. (2010). Peptide-Based Probes for Targeted Molecular Imaging. *Biochemistry* 49, 1364–1376. doi:10.1021/bi901135x

León-Janampa, N., Zimic, M., Shinkaruk, S., Quispe-Marcatoma, J., Gutarra, A., Le Bourdon, G., et al. (2020). Synthesis, Characterization and Bio-Functionalization of Magnetic Nanoparticles to Improve the Diagnosis of Tuberculosis. *Nanotechnology* 31, 175101. doi:10.1088/1361-6528/ab6ab1

Li, J., He, Y., Sun, W., Luo, Y., Cai, H., Pan, Y., et al. (2014). Hyaluronic Acid-Modified Hydrothermally Synthesized Iron Oxide Nanoparticles for Targeted Tumor MR Imaging. *Biomaterials* 35, 3666–3677. doi:10.1016/j.biomaterials.2014.01.011

Li, J., Zheng, L., Cai, H., Sun, W., Shen, M., Zhang, G., et al. (2013). Polyethyleneimine-mediated Synthesis of Folic Acid-Targeted Iron Oxide Nanoparticles for *In Vivo* Tumor MR Imaging. *Biomaterials* 34, 8382–8392. doi:10.1016/j.biomaterials.2013.07.070

Li, Z., Wang, C., Cheng, L., Gong, H., Yin, S., Gong, Q., et al. (2013). PEG-functionalized iron oxide nanoclusters loaded with chlorin e6 for targeted, NIR light induced, photodynamic therapy. *Biomaterials* 34, 9160–9170. doi:10.1016/j.biomaterials.2013.08.041

Liu, G., Xie, J., Zhang, F., Wang, Z., Luo, K., Zhu, L., et al. (2011). N-Alkyl-PEI-functionalized Iron Oxide Nanoclusters for Efficient siRNA Delivery. *Small* 7, 2742–2749. doi:10.1002/smll.201100825

Lohrke, J., Frenzel, T., Endrikat, J., Alves, F. C., Grist, T. M., Law, M., et al. (2016). 25 Years of Contrast-Enhanced MRI: Developments, Current Challenges and Future Perspectives. *Adv. Ther.* 33, 1–28. doi:10.1007/s12325-015-0275-4

Luo, Y., Li, Y., Li, J., Fu, C., Yu, X., and Wu, L. (2019). Hyaluronic Acid-Mediated Multifunctional Iron Oxide-Based MRI Nanoprobes for Dynamic Monitoring of Pancreatic Cancer. *RSC Adv.* 9, 10486–10493. doi:10.1039/c9ra00730j

Luo, Y., Yang, J., Yan, Y., Li, J., Shen, M., Zhang, G., et al. (2015). RGD-functionalized Ultrasmall Iron Oxide Nanoparticles for Targeted T_1-weighted MR Imaging of Gliomas. *Nanoscale* 7, 14538–14546. doi:10.1039/c5nr04003e

Ma, D., Chen, J., Luo, Y., Wang, H., and Shi, X. (2017). Zwitterion-coated Ultrasmall Iron Oxide Nanoparticles for Enhanced T_1-Weighted Magnetic Resonance Imaging Applications. *J. Mater Chem. B* 5, 7267–7273. doi:10.1039/c7tb01588g

Maeda, H. (2010). Tumor-Selective Delivery of Macromolecular Drugs *via* the EPR Effect: Background and Future Prospects. *Bioconjug Chem.* 21, 797–802. doi:10.1021/bc100070g

Martinkova, P., Brtnicky, M., Kynicky, J., and Pohanka, M. (2018). Iron Oxide Nanoparticles: Innovative Tool in Cancer Diagnosis and Therapy. *Adv. Healthc. Mater* 7, 1700932. doi:10.1002/adhm.201700932

Mcbain, S. C., Yiu, H. H. P., El Haj, A., and Dobson, J. (2007). Polyethyleneimine Functionalized Iron Oxide Nanoparticles as Agents for DNA Delivery and Transfection. *J. Mat. Chem.* 17, 2561–2565. doi:10.1039/b617402g

Mitchell, M. J., Billingsley, M. M., Haley, R. M., Wechsler, M. E., Peppas, N. A., and Langer, R. (2021). Engineering Precision Nanoparticles for Drug Delivery. *Nat. Rev. Drug Discov.* 20, 101–124. doi:10.1038/s41573-020-0090-8

Naha, P. C., Liu, Y., Hwang, G., Huang, Y., Gubara, S., Jonnakuti, V., et al. (2019). Dextran-Coated Iron Oxide Nanoparticles as Biomimetic Catalysts for Localized and pH-Activated Biofilm Disruption. *Acs Nano* 13, 4960–4971. doi:10.1021/acsnano.8b08702

Oliveira, O. N., Iost, R. M., Siqueira, J. R., Crespilho, F. N., and Caseli, L. (2014). Nanomaterials for Diagnosis: Challenges and Applications in Smart Devices Based on Molecular Recognition. *ACS Appl. Mater Interfaces* 6, 14745–14766. doi:10.1021/am5015056

Shen, Z., Wu, A., and Chen, X. (2017). Iron Oxide Nanoparticle Based Contrast Agents for Magnetic Resonance Imaging. *Mol. Pharm.* 14, 1352–1364. doi:10.1021/acs.molpharmaceut.6b00839

Shi, S. F., Jia, J. F., Guo, X. K., Zhao, Y. P., Chen, D. S., Guo, Y. Y., et al. (2012). Biocompatibility of Chitosan-Coated Iron Oxide Nanoparticles with Osteoblast Cells. *Int. J. Nanomedicine* 7, 5593–5602. doi:10.2147/IJN.S34348

Shi, X., Wang, S. H., Swanson, S. D., Ge, S., Cao, Z., Van Antwerp, M. E., et al. (2008). Dendrimer-functionalized Shell-Crosslinked Iron Oxide Nanoparticles for *In-Vivo* Magnetic Resonance Imaging of Tumors. *Adv. Mat.* 20, 1671–1678. doi:10.1002/adma.200702770

Sim, A. J., Kaza, E., Singer, L., and Rosenberg, S. A. (2020). A Review of the Role of MRI in Diagnosis and Treatment of Early Stage Lung Cancer. *Clin. Transl. Radiat. Oncol.* 24, 16–22. doi:10.1016/j.ctro.2020.06.002

Souri, M., Soltani, M., Moradi Kashkooli, F., Kiani Shahvandi, M., Chiani, M., Shariati, F. S., et al. (2022). Towards Principled Design of Cancer Nanomedicine to Accelerate Clinical Translation. *Mater Today Bio* 13, 100208. doi:10.1016/j.mtbio.2022.100208

Swierczewska, M., Han, H. S., Kim, K., Park, J. H., and Lee, S. (2016). Polysaccharide-based Nanoparticles for Theranostic Nanomedicine. *Adv. Drug Deliv. Rev.* 99, 70–84. doi:10.1016/j.addr.2015.11.015

Tassa, C., Shaw, S. Y., and Weissleder, R. (2011). Dextran-Coated Iron Oxide Nanoparticles: A Versatile Platform for Targeted Molecular Imaging, Molecular Diagnostics, and Therapy. *Acc. Chem. Res.* 44, 842–852. doi:10.1021/ar200084x

Toole, B. P. (2004). Hyaluronan: From Extracellular Glue to Pericellular Cue. *Nat. Rev. Cancer* 4, 528–539. doi:10.1038/nrc1391

Wahsner, J., Gale, E. M., Rodríguez-Rodríguez, A., and Caravan, P. (2019). Chemistry of MRI Contrast Agents: Current Challenges and New Frontiers. *Chem. Rev.* 119, 957–1057. doi:10.1021/acs.chemrev.8b00363

Wei, H., Bruns, O. T., Kaul, M. G., Hansen, E. C., Barch, M., Wiśniowska, A., et al. (2017). Exceedingly Small Iron Oxide Nanoparticles as Positive MRI Contrast Agents. *Proc. Natl. Acad. Sci. U. S. A.* 114, 2325–2330. doi:10.1073/pnas.1620145114

Xiao, B., Han, M. K., Viennois, E., Wang, L., Zhang, M., Si, X., et al. (2015). Hyaluronic Acid-Functionalized Polymeric Nanoparticles for Colon Cancer-Targeted Combination Chemotherapy. *Nanoscale* 7, 17745–17755. doi:10.1039/c5nr04831a

Yallapu, M. M., Foy, S. P., Jain, T. K., and Labhasetwar, V. (2010). PEG-Functionalized Magnetic Nanoparticles for Drug Delivery and Magnetic Resonance Imaging Applications. *Pharm. Res.* 27, 2283–2295. doi:10.1007/s11095-010-0260-1

Yu, W. W., Chang, E., Sayes, C. M., Drezek, R., and Colvin, V. L. (2006). Aqueous Dispersion of Monodisperse Magnetic Iron Oxide Nanocrystals through Phase Transfer. *Nanotechnology* 17, 4483–4487. doi:10.1088/0957-4484/17/17/033

Zhang, N., Wang, Y., Zhang, C., Fan, Y., Li, D., Cao, X., et al. (2020). LDH-stabilized Ultrasmall Iron Oxide Nanoparticles as a Platform for Hyaluronidase-Promoted MR Imaging and Chemotherapy of Tumors. *Theranostics* 10, 2791–2802. doi:10.7150/thno.42906

Zhao, N. N., Yan, L. M., Xue, J. J., Zhang, K., and Xu, F. J. (2021). Degradable One-Dimensional Dextran-Iron Oxide Nanohybrids for MRI-Guided Synergistic Gene/photothermal/magnetolytic Therapy. *Nano Today* 38, 101118. doi:10.1016/j.nantod.2021.101118

Zhi, J., Wang, Y., Lu, Y., Ma, J., and Luo, G. (2006). *In Situ* preparation of Magnetic chitosan/Fe_3O_4 Composite Nanoparticles in Tiny Pools of Water-In-Oil Microemulsion. *React. Funct. Polym.* 66, 1552–1558. doi:10.1016/j.reactfunctpolym.2006.05.006

Zhou, X., He, C., Liu, M., Chen, Q., Zhang, L., Xu, X., et al. (2021). Self-assembly of Hyaluronic Acid-Mediated Tumor-Targeting Theranostic Nanoparticles. *Biomater. Sci.* 9, 2221–2229. doi:10.1039/d0bm01855d

Conflict of Interest: The authors declare that the research was conducted in the absence of any commercial or financial relationships that could be construed as a potential conflict of interest.

Publisher's Note: All claims expressed in this article are solely those of the authors and do not necessarily represent those of their affiliated organizations, or those of the publisher, the editors, and the reviewers. Any product that may be evaluated in this article, or claim that may be made by its manufacturer, is not guaranteed or endorsed by the publisher.